frontiers in Neural Circuits

ORIGINAL RESEARCH
published: 21 July 2017
doi: 10.3389/fncir.2017.00050

Visually Driven Neuropil Activity and Information Encoding in Mouse Primary Visual Cortex

Sangkyun Lee[1,2*†], *Jochen F. Meyer*[3†], *Jiyoung Park*[3] *and Stelios M. Smirnakis*[1,2,4*]

[1] Department of Neurology, Brigham and Women's Hospital, Boston, MA, United States, [2] Harvard Medical School, Boston, MA, United States, [3] Department of Neurology, Baylor College of Medicine, Houston, TX, United States, [4] Veterans Administration Hospital, Boston, MA, United States

Cortical neuropil modulations recorded by calcium imaging reflect the activity of large aggregates of axo-dendritic processes and synaptic compartments from a large number of neurons. The organization of this activity impacts neuronal firing but is not well understood. Here we used *in vivo* 2-photon imaging with Oregon Green Bapta (OGB) and GCaMP6s to study neuropil visual responses to moving gratings in layer 2/3 of mouse area V1. We found neuropil responses to be strongly modulated and more reliable than neighboring somatic activity. Furthermore, stimulus independent modulations in neuropil activity, i.e., noise correlations, were highly coherent across the cortical surface, up to distances of at least 200 μm. Pairwise neuropil-to-neuropil-patch noise correlation strength was much higher than cell-to-cell noise correlation strength and depended strongly on brain state, decreasing in quiet wakefulness relative to light anesthesia. The profile of neuropil noise correlation strength decreased gently with distance, dropping by ~11% at a distance of 200 μm. This was comparatively slower than the profile of cell-to-cell noise correlations, which dropped by ~23% at 200 μm. Interestingly, in spite of the "salt & pepper" organization of orientation and direction encoding across mouse V1 neurons, populations of neuropil patches, even of moderately large size (radius ~100 μm), showed high accuracy for discriminating perpendicularly moving gratings. This was commensurate to the accuracy of corresponding cell populations. The dynamic, stimulus dependent, nature of neuropil activity further underscores the need to carefully separate neuropil from cell soma activity in contemporary imaging studies.

Keywords: neuropil, visual cortex, population codes, visual system, information encoding

OPEN ACCESS

Edited by:
Edward S. Ruthazer, McGill University, Canada

Reviewed by:
Tobias Rose, Max Planck Institute of Neurobiology (MPG), Germany
Carey Y. L. Huh, University of California, Irvine, United States

***Correspondence:**
Sangkyun Lee
lee.sangkyun@gmail.com
Stelios M. Smirnakis
smsmirnakis@partners.org

[†] *These authors have contributed equally to this work.*

Received: *14 March 2017*
Accepted: *30 June 2017*
Published: *21 July 2017*

Citation:
Lee S, Meyer JF, Park J and Smirnakis SM (2017) Visually Driven Neuropil Activity and Information Encoding in Mouse Primary Visual Cortex. Front. Neural Circuits 11:50. doi: 10.3389/fncir.2017.00050

INTRODUCTION

Chklovskii et al. (2002) and Braitenberg et al. (Braitenberg and Shchuz, 1998) argued that axons (including axonal boutons) and dendrites constitute ~70–80% of the neuropil. Neuropil activity reflects chiefly aggregate activity from axonal and dendritic branches as well as pre- and post-synaptic components in large numbers of local synaptic aggregates. Individual neurons fire in the context of nearby neuropil activity. It is therefore important to understand more about the neuropil's functional organization. Kerr and colleagues measured the spontaneous calcium signal modulation in large ~10,000 μm^2 patches of neuropil in layer 2/3 of rat motor and barrel cortices

(Kerr et al., 2005) and showed that it correlates well with the simultaneously recorded electro-corticogram (ECoG). Other studies (Kerlin et al., 2010; Bonin et al., 2011; Chen et al., 2013) document but do not systematically quantify visually driven neuropil responses (c.f., Goltstein et al., 2015). It is interesting to understand how the spatial organization of neuropil activity relates to the activity of nearby neurons during visual processing. Mouse primary visual cortex is thought to have "salt & pepper" organization for orientation selectivity (Ohki et al., 2005; but see Ringach et al., 2016). It is not clear whether this organization is also reflected in the neuropil, or whether the neuropil has more coarse grained orientation representation allowing large neuropil neighborhoods to have significant residual orientation preference. More generally, it is important to know how strongly correlated somatic activity is to adjacent neuropil activity and how reliable neuropil visual responses are compared to adjacent neuronal responses.

We recorded neuronal activity using *in vivo* two-photon calcium imaging in layer 2/3 of mouse primary visual cortex (V1) while presenting drifting grating stimuli subtending a large visual angle. Our experiments reveal that local neuropil patches exhibit stronger and more reliable calcium responses to visual stimulation than adjacent neurons, and this difference is more pronounced under anesthesia than during quiet wakefulness. Neuropil activity is highly correlated across the field of view but correlation strength decays slowly as a function of distance up to the range examined ($\sim$200 μm). Neuropil correlation strength depends on brain state, being higher under light anesthesia compared to quiet wakefulness. Finally, somewhat surprisingly because of the "salt & pepper" mouse V1 organization, relatively large ($\sim 15 \times 15$ μm^2 or larger) neuropil patches show high decoding accuracies in a direction discrimination paradigm, on par with the performance of nearby cell populations. This suggests that in layer 2/3 of mouse V1, substantial local direction information is contained in the aggregate activity of neuropil patches with radii ranging from 30 to as large as 200 μm.

MATERIALS AND METHODS

Animal Preparation

All experiments and animal procedures were performed in accordance with guidelines of the National Institutes of Health for the care and use of laboratory animals and were approved by the IACUC at Baylor College of Medicine. All mice used were derived from C57BL/6 lines and were 4–8 weeks old. Imaging experiments under anesthesia were performed in 5 fields of view (FOV's) from 3 Parvalbumin (PV)-Cre X Ai9 F1 mice and 2 FOV's from 2 Dlx5/6-Cre X Ai9 F1 mice. Awake experiments were performed in 11 FOV's (2 FOV's from 2 PV-Cre X Ai9 F1 mice and 9 FOV's from 4 wild-type C57BL6 mice). For GCaMP6s (Chen et al., 2013) experiments two Thy1-GCaMP6s 4.3 (Dana et al., 2014) mice, which express GCaMP6 genetically, were used.

Surgery

All procedures were carried out according to animal welfare guidelines authorized by the Baylor College of Medicine IACUC committee. All surgeries were performed under general anesthesia with 1.5% isoflurane. The mouse head was fixed in a stereotactical stage (Kopf Instruments), and eyes were protected with a thin layer of polydimethylsiloxane (30,000 cst, Sigma-Aldrich). After removing the scalp, a custom-made titanium headplate was attached to the skull with dental acrylic (Lang Dental). A 3 mm wide circular craniotomy centered 2.5 mm lateral of the midline and 1.2 mm anterior of the lambda suture was made, targeting the middle of the monocular region of left V1. A coverglass with a hole for pipette access was placed on the brain and carefully anchored with vetbond glue (3M, Saint Paul, MN) and dental acrylic (Lang Dental).

Dye Loading and Imaging

We used the calcium indicator Oregon Green BAPTA-1 (OGB) because it stains uniformly both cell bodies and aggregate neuropil processes near the site of injection. Fifty micrograms Oregon Green 488 BAPTA-1 AM (OGB, Invitrogen) was dissolved in 4 μl DMSO (heated to 40°C) with 10% Pluronic acid F-127 (Invitrogen), vortexed for 20 min, and diluted in 40 μl 0.9%-NaCl solution containing 10 μM Alexa-594 for experiments with tdTomato-labeled interneurons, and 10 μM Sulforhodamine 101 (Nimmerjahn et al., 2004) for selective astrocyte-labeling in other experiments. This solution was injected using a glass pipette at depths of 200, 300, and 400 μm of mouse visual cortex under two-photon visual guidance. Cell imaging commenced 1 h after the dye injection. Populations of 50–100 cells located 150–250 μm below the pia were imaged with water-dipping objective lenses, either 20x, 0.95 NA (Olympus), or 25x, 1.1 NA (Nikon), in a modified Prairie Ultima IV two-photon laser scanning microscope (Prairie Technologies, Middleton, WI), fed by a Chameleon Ultra II laser (Coherent, Santa Clara, CA). Local windows of 200–250 $\times$ 200–250 μm with an in-plane iso-symmetric pixel resolution of 1.2–1.9 μm were imaged at frame rates of 7–10 Hz. Depending on imaging depth, the laser power was kept between 10 mW at the surface and 50 mW at depths below 250 μm, at 840 nm (when the patch pipette was filled with Alexa 594 or sulforhodamine) or 890 nm (when filled with dextran) laser wavelength. During visual stimulation experiments under light anesthesia, 0.7% isoflurane was maintained during the experiment via a nose cone and anesthesia was monitored between imaging sessions via the eyelid reflex. The body temperature of the mouse was kept at 36–37°C with a heating pad (Harvard Apparatus).

For experiments with GCaMP6s, the craniotomy was covered with a glass window on the center of mouse visual cortex −2.7 mm lateral to the midline and 1.5 mm posterior to the bregma. Imaging experiments were performed 1–2 weeks after the surgery. In these experiments, the laser power was set similarly to OGB experiments but the wavelength was set to 920 nm. Populations of 100–200 cells in layer 2/3 of mouse V1 were simultaneously imaged with a large FOV ($\sim$400 $\times$ 400 μm) 0.5–1 h after injecting a sedating cocktail consisting of 1.5 mg/kg of fentanyl and 0.5 mg/kg dexmedetomidine.

For both anesthetized and sedated animals, silicone oil (polydimethylsiloxane-200, Sigma-Aldrich) was applied to both eyes during experiments. For awake experiments, while animals

were restrained with a head post, they were free to move forward or backward on a rotating wheel.

Visual Stimulation

Visual stimuli were generated in MATLAB and displayed using Psychtoolbox (Brainard, 1997). The stimuli were presented on an LCD monitor (DELL 2408WFP, Dell, Texas, USA) at 60 Hz frame rate, positioned 32 cm in front of the right eye, centered at 45° clockwise from the mouse's body axis. The visual angle of the screen spanned 54° elevation and 78° azimuth. The screen was gamma-corrected, and the mean luminance level was photopic at 80 cd/m^2. Our visual stimulation paradigm consisted of grating stimuli moving in one of 2 orthogonal directions (0 vs. 90°) at 3 different contrast levels (100, 40, 15% Michelson contrast; Michelson, 1927). Each grating stimulus was generated as a square wave with a spatial frequency of 0.04 cycles/degree and a temporal frequency of 2 Hz. Grating stimuli were presented for 600 ms (500 ms for a single FOV) followed by an inter-stimulus interval of 1.5 s during which a full-field gray screen at the same mean luminance (background illumination) was presented. Each of the 6 possible conditions was presented 80–100 times in pseudo-random interleaved order.

For experiments with animals expressing GCaMP6s genetically, grating stimuli were presented for 500 ms at 100 and 40% contrast, followed by an inter-stimulus interval of 1.5 s.

Patch-Clamp Recording

Whole-cell and loose-patch recordings were obtained with a Heka EPC-10 USB amplifier in current-clamp mode using standard techniques (Margrie et al., 2003). Glass pipettes of 6–8 MOhm, filled with intracellular solution (in mM: 105 K-gluconate, 30 KCl, 10 HEPES, 10 phosphocreatine, 4 ATPMg, and 0.3 GTP), adjusted to 290 mOsm and pH 7.3 with KOH (Golshani et al., 2009) and containing 10 μM Alexa-594 or tetramethylrhodamine dextran (Invitrogen), were used for the recording under two-photon visual guidance. After approaching a target cell with pressure adjustment based on the depth of the pipette from the pia and the distance to the cell, a GigaOhm seal between cell membrane and the pipette was formed. A patch of cell membrane was broken by applying 200 ms pulses of negative pressure with increasing strength using a picospritzer III (Parker Hannifin, Pine Brook, NJ). Fast pipette capacitance was neutralized before break-in, and slow capacitance afterwards. We targeted putative pyramidal cells in layer 2/3 (between 100 and 250 μm below the pia). We performed the patch-clamping experiments *in vivo*, while presenting moving oriented grating stimuli, whose orientation varied randomly in steps of 30°. Stimulus presentation duration was 1 s followed by an inter-stimulus interval of 1.5 s. The recording time for each cell was 5–10 min and mean firing rate over the entire recording time ranged from 0.8 to 5 Hz.

Data Analysis

Preprocessing

Movies were motion-corrected along a 2D image plane (x-y motion). Motion parameters were estimated in the red channel, in which tdTomato-labeled interneurons were identified, by registering all image frames to the average of the first 5 image frames using a sub-pixel registration method (Guizar-Sicairos et al., 2008). Then, the correction parameters were applied to the green channel (in which calcium dynamics of cells were monitored) to reconstruct motion-corrected movies. Data from awake animals were further constrained based on the extent of their movements during imaging. Animal movement during awake experiments was indirectly measured by monitoring XY movements of the FOV imaged. All trials showing any image frame with movement $>2 \times$ pixel size ($\sim$3 μm within the x-y plane) from the first frame of each movie, or >0.5 pixel ($\sim$0.7 μm) in consecutive frames were excluded from data analysis. The motion threshold used to select awake data resulted in similar x-y motion levels (i.e., <3 microns) during quiet wakefulness as were observed under anesthesia. Hereafter, "awake data" refers to data acquired while animals were standing still (quiet wakefulness).

The application of this criterion reduced the number of trials per condition to $\sim$70 but minimized the possibility that different results between the different brain states were due to motion artifacts.

For cell identification, a local region-of-interest (ROI) over a cell body was manually defined with a circular disk to cover the cell body, then scanned for the pixel with the highest fluorescence value within the disk (cell body center). The boundary of the region containing the cell signal was then defined by thresholding at $0.5 \times$ maximum fluorescence within the disk along the polar coordinates (**Figure 1A**; Chen et al., 2013). To correct for slow signal drift over time, the signal time series from each pixel was high-pass filtered (HPF) at 0.05 Hz using the discrete cosine transformation.

We corrected for optical contamination from the neuropil signal to the cell soma. Note that this is important to do since optical contamination extends considerably further along the Z-axis (see **Figure 1B**) compared to within the X-Y plane, and the neuropil signal surrounds the soma. Since the neuropil signal is locally uniform, changing only slowly with cortical distance (**Figures 4A**, **5B** right), it is possible to do this by subtracting the neuropil signal surrounding the cell in the image plane. In contrast, doing the converse correction, i.e., correcting for contamination from the cell soma to nearby neuropil signal was not necessary: (1) the optical spread is much smaller along the X-Y plane (in our data the standard deviation of the point spread function along the X-Y plane was $\sim$0.22 μm), (2) neuropil patches were shaped like rings surrounding the cells, with inner diameter $>\sim$7 μm from the cell center, at least $\sim$2 μm further away from the cell border. In addition, linear subtraction of cell activity from neuropil signal (see section for calculation of neuropil noise correlations) did not change our main conclusions on neuropil activity (see **Figure 4C** and Supplementary Figure 5A).

We measured the ratio between the mean calcium signal within the lumen of non-radial blood vessels ($\leq$10 μm) and the surrounding neuropil patch (Kerlin et al., 2010). This gave us an approximate measure of neuropil contamination at the cell soma, the so-called contamination scale, whose typical value was 0.6.

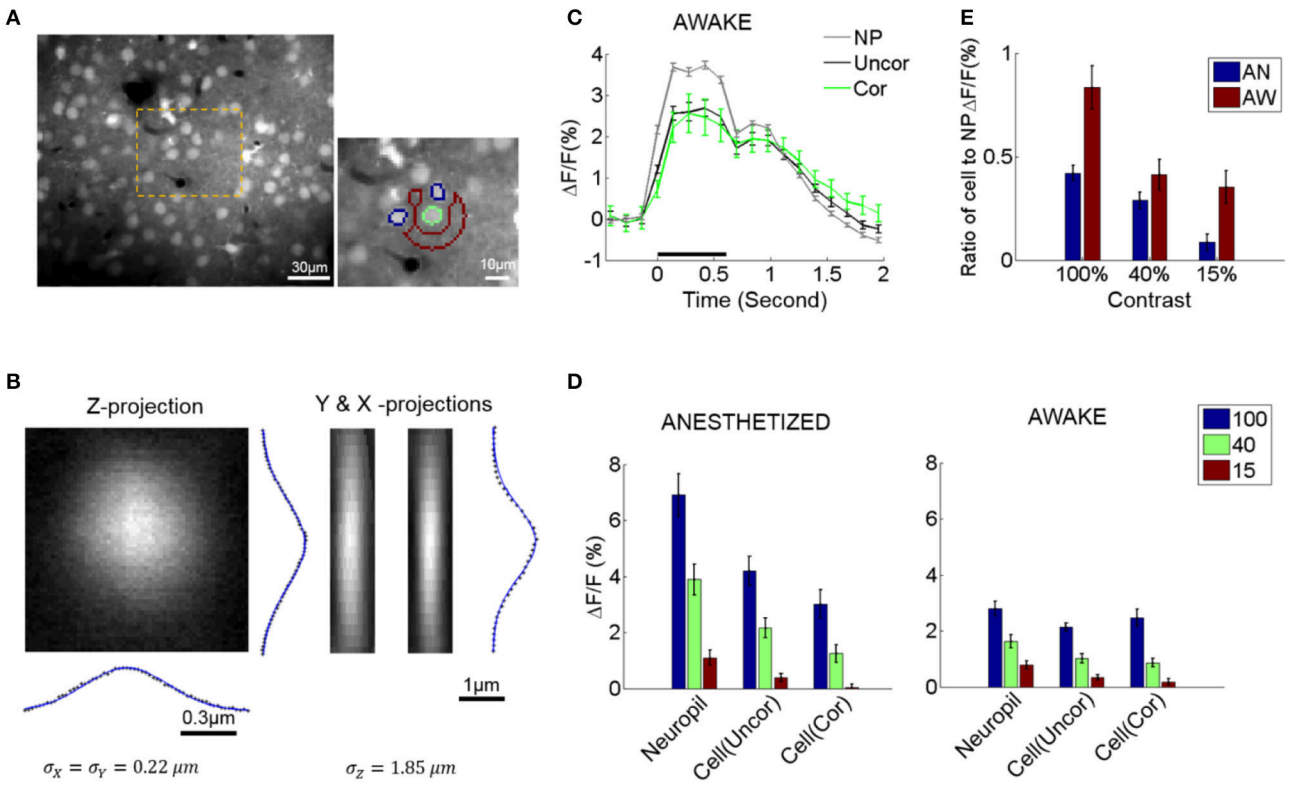

FIGURE 1 | Neuropil and somatic response variability and dependence to contrast. **(A)** Selecting cell somata and local neuropil patches. An example of a typical field of view (FOV, left). The orange area is magnified on the right. Cell radii in our experiments were generally ≤5 μm. A local neuropil patch was defined around each cell body as an annulus with inner radius 7 μm and outer radius 15 μm. Any annulus pixels belonging to or being close to other cells (i.e., within 7 μm of the cell center), vessels, or poorly stained regions were excluded by visual inspection to minimize contamination of the neuropil signal by sources other than neuropil. In the example, the green outline shows a selected cell soma (green outline only for visualization). Its local neuropil patch is outlined in red. Note that nearby neurons were excluded from the definition of the neuropil ROI (annulus) and are shown in blue (outline only). The pixel resolution is 1.2 × 1.2 μm. **(B)** Gaussian fit of the point spread function (PSF) of our microscope measured by imaging a single spherical fluorophore with a radius of 0.1 μm. **(C)** Example of the average response of cells and neuropil-patches (annular patch with radii of 7–15 μm) in a single FOV to 100% contrast. "NP": mean neuropil response. "Uncor": mean uncorrected somatic response. "Cor": mean somatic response after neuropil contamination correction (see Section Materials and Methods) **(D)** Mean evoked fluorescence responses to gratings of 100, 40, and 15% contrast, respectively, derived from all visually responsive cells in 7 anesthetized (AN) and 11 awake (AW) FOV's, respectively. **(E)** Ratio of mean somatic vs. mean neuropil responses (pooled from all FOV data). These ratios are plotted after correcting for neuropil contamination. Note that the relative strength of cell vs. neuropil ΔF/F responses decreased in the lightly anesthetized state. This is largely due to the fact that neuropil responses markedly increase in the lightly anesthetized state. NP, neuropil; AW, awake state; AN, anesthetized state. Statistics are across FOV's.

To correct for the neuropil contamination at the soma, the mean fluorescence of the adjacent neuropil patch, F_n, was subtracted using the contamination scale S: $F_{correct} = F - S^*F_n$. The patch F_n formed an annulus with a radius of 7–15 μm centered around the soma, excluding pixels that belonged to other cell bodies or astrocytes, which are labeled red with sulforhodamine (**Figure 1A**). In our calcium imaging setup, the point spread function is wider along the z-axis (**Figure 1B**), so the correction factor mostly compensates for neuropil contamination along the z-axis. The contamination of the neuronal signal by the neuropil signal varied with cell size as well as with the in-plane diameter of the soma cross-section. We therefore examined a range of values around the empirically estimated value $S = 0.5$–0.6, and verified that reasonable variation in the level of contamination (S) did not significantly affect our conclusions (**Figures 1C,D** and Supplementary Figure 1). We found that a range of correction factors S ($S = 0.4$–0.6) result in similar response patterns as shown in **Figures 1C,D** and Supplementary Figure 5A. Higher levels of contamination ($S = 0.8$) began to distort visually evoked responses, resulting in prolonged, non-physiological, delays of the visual response peak (Supplementary Figures 1A,B,D,E). Such high levels of contamination were not empirically found in our data, as judged by measuring the spread of the calcium signal into the lumen of vessels running parallel or perpendicular to the field of view, whose lumens were commensurate to the typical range of cell sizes.

Effects of Correction on Noise Correlations

The neuropil correction naturally decreases somewhat the magnitude of the cell ΔF/F response as it removes the component of it that is due to neuropil contamination (**Figure 1**, Supplementary Figure 1). This decrease is mainly evident in the anesthetized state, where the neuropil response is relatively higher. The main effect of the neuropil correction however,

is in allowing a veridical estimation of noise correlation strength. Prior to neuropil contamination correction, mean inter-neuronal noise correlation coefficients ranged from ∼0.15 to 0.3 (Supplementary Figure 2), commensurate with results from several published 2-photon imaging studies (Kerr et al., 2007; Golshani et al., 2009; Rothschild et al., 2010). Such measurements are subject to neuropil contamination, which, because of its high spatial coherence, has the potential to substantially alter the magnitude of noise correlations. Neuropil contamination correction results in a significant adjustment resulting in noise correlation coefficients ∼0.05 (Supplementary Figure 2). Note that we calculated the noise correlation by estimating the spike rates from the corrected neuropil signal (see below for spike-rate estimation). These values are much closer to values (<0.05) reported in recent electrophysiology studies (Ecker et al., 2010, 2014), which had excellent single unit isolation and recording stability. In conclusion, while the correction for neuropil contamination has little effect on mean neuronal visual responses, it does have a big effect on the strength of noise correlations across pairs of cells.

Note that unless explicitly mentioned, all cell responses are calculated by implementing a neuropil contamination correction with the empirically determined factor $S = 0.6$.

Only putative excitatory pyramidal neurons and their surrounding neuropil patches were used in analysis. Interneurons expressing Td-tomato and astrocytes (stained red with sulforhodamine) were excluded from the analysis.

A New, Stable, Spike-Estimation Algorithm Outperforming (Vogelstein et al., 2010)

We used a new method based on sparse non-negative linear regression to estimate spike rates associated with the calcium fluorescence ΔF/F signal. This method assumes linear calcium dynamics with a time constant that does not change over the course of the experiment. Cell firing is modeled as causing an instant (within one ∼130 ms frame) calcium increase that slowly decays in the subsequent frames:

$$c_t = rc_{t-1} + n_{t-1} \tag{1}$$

where c is the cell's calcium ΔF/F signal, t indexes time in units of ∼130 ms frames, $r = 1 - \Delta/\tau$, where Δ is the frame duration, τ the time constant and n the normalized spike number during the frame duration, which has the same units as ΔF/F.

In Matrix-vector form,

$$\begin{bmatrix} -r & 1 & 0 & \dots & 0 \\ 0 & -r & 1 & 0 & \dots & 0 \\ \vdots & & & \ddots & & \vdots \\ & & 0 & -r & 1 & 0 \\ 0 & & \dots & 0 & -r & 1 \end{bmatrix} \begin{bmatrix} c_1 \\ \vdots \\ c_t \\ \vdots \\ c_T \end{bmatrix} \begin{bmatrix} n_1 \\ \vdots \\ n_t \\ \vdots \\ n_T \end{bmatrix}$$

$$\boldsymbol{M}C = \boldsymbol{n} \tag{2}$$

where $\boldsymbol{M}$ is a convolution matrix that transforms a calcium concentration time series to spikes, and $\boldsymbol{n} \geq \mathbf{0}$.

Or

$$\boldsymbol{C} = \boldsymbol{P}n \tag{3}$$

where $\boldsymbol{P}$ is the inverse matrix of $\boldsymbol{M}$, and $\boldsymbol{n} \geq \mathbf{0}$.

Assuming exponential distribution of spikes, the objective function for $\boldsymbol{n}$ is defined as a minimum mean square error form:

$$J = \|\boldsymbol{C} - \boldsymbol{P}n\|_{\mathbf{F}}^2 + k\|\boldsymbol{n}\|_{\mathbf{1}} \; s.t. \; \boldsymbol{n} \geq \mathbf{0} \tag{4}$$

where k is a regularization parameter.

After incorporating a term ($\boldsymbol{a} \geq \mathbf{0}$) that allows us to optimize the spatial filtering of the pixels within the cell body, this formula becomes:

$$J = \left\| \boldsymbol{C} - \boldsymbol{P}n\boldsymbol{a}^T \right\|_{\boldsymbol{F}}^2 + k_1\|\boldsymbol{n}\|_{\mathbf{1}} + k_2\|\boldsymbol{a}\|_{\mathbf{1}} \; s.t. \; \boldsymbol{n} \geq \mathbf{0} \; and \; \boldsymbol{a} \geq \mathbf{0}. \tag{5}$$

$\boldsymbol{C}$ is now a multi-pixel Matrix (time samples × pixels), and the spatial filter $\boldsymbol{a}$ is constrained to be non-negative and to be bounded for convergence of the objective function. Here we adopted the L_1-norm ($\|\|_1$) minimization to bound $\boldsymbol{a}$ and $\boldsymbol{n}$ guaranteeing the convergence of the alternating optimization algorithm (between n and a). The advantage of the regularization used for $\boldsymbol{a}$ is to minimize contributions of low SNR pixels to spike estimation.

To estimate $\boldsymbol{n}$ and $\boldsymbol{a}$ iteratively, we used an optimization method similar to the Expectation Maximization algorithm (Dempster et al., 1997), alternately estimating $\boldsymbol{n}$ while holding $\boldsymbol{a}$ fixed and vice versa:

$$J(\boldsymbol{n}) = \left\| \mathbf{C} - \boldsymbol{P}n\mathbf{a}^T \right\|_{\boldsymbol{F}}^2 + k_1\|\boldsymbol{n}\|_{\mathbf{1}}, s.t. \; \boldsymbol{n} \geq \mathbf{0} \tag{6}$$

$$J(\boldsymbol{a}) = \left\| \mathbf{C} - \boldsymbol{P}n\mathbf{a}^T \right\|_{\boldsymbol{F}}^2 + k_2\|\boldsymbol{a}\|_{\mathbf{1}}, s.t. \; \boldsymbol{a} \geq \mathbf{0} \tag{7}$$

This model can also be interpreted as a Bayesian model, maximizing the a posterior probability

$$p\,(\boldsymbol{C} |\; \boldsymbol{n}, \boldsymbol{a})\, p\,(\boldsymbol{n})\, p(\boldsymbol{a}) \tag{8}$$

$$\text{where } p\,(\boldsymbol{C} |\; \boldsymbol{n}, \boldsymbol{a}) = 1/(2\pi\lambda_0)^{\frac{N}{2}} \exp\left(\frac{\left\| \mathbf{C} - \boldsymbol{P}n\boldsymbol{a}^T \right\|_{\boldsymbol{F}}^2}{\lambda_0}\right), \tag{9}$$

$$\text{with priors } \mathrm{p}(\boldsymbol{n}) = \lambda_1 \exp(-\lambda_1 \boldsymbol{n}), \boldsymbol{n} \geq \mathbf{0} \tag{10}$$

$$\text{and } p(\boldsymbol{a}) = \exp(-\boldsymbol{a}), \boldsymbol{a} \geq \mathbf{0} \tag{11}$$

From the Bayesian model, the parameter k_1 and k_2 can be released freely by maximizing the posterior probability. Specifically, this was performed by alternatively updating $\boldsymbol{C}$, $\boldsymbol{n}$, and $\mathbf{a}$ and updating only λ_0 with λ_1 fixed. In our estimation, λ_1 was set as the imaging frame period. Therefore, for Equations (6, 7), both parameters, k_1 and k_2, can be controlled solely with λ_0.

In each iteration, after estimating $\boldsymbol{n}$ and $\boldsymbol{a}$, λ_0 can be updated by maximizing

$$p\,(\boldsymbol{C} \mid\; \lambda_0) = \int p\,(\boldsymbol{C} \mid\; \boldsymbol{n}, \boldsymbol{a}, \lambda_0)\, p\,(\boldsymbol{n})\, p\,(\boldsymbol{a})\, d\boldsymbol{a}d\boldsymbol{n}. \tag{12}$$

However, due to the intractability of the integral, it is a common practice to obtain the λ_0 estimate by setting the derivative of the

log-posterior probability, $\log(p(\boldsymbol{C} \mid \boldsymbol{n}, \boldsymbol{a})\, p(\boldsymbol{n})\, p(\boldsymbol{a}))$, with respect to λ_0 equal to 0 and then solving the equation.

We used an optimization technique for the linear regression model with the L_1 norm, which uses a log-barrier technique for non-negative constraints and tests for convergence of the learning algorithm via assessing the gap between primal and dual problems (Boyd and Vandenberghe, 2004; Kim et al., 2007). This convex optimization with completely bounding alternative parameters theoretically converges to the global minimum (Grippo and Sciandrone, 2000; Kim and Park, 2007).

Our spike estimation method, like a previously published method (Vogelstein et al., 2010), assumes linear calcium dynamics and an exponential distribution of spike rates, and uses alternating optimization and the log-barrier optimization technique for L_1-norm minimization. However, it has one major advantage over (Vogelstein et al., 2010), which is that its parameter optimization is stable. Theoretically, interacting parameters could cause the objective (cost) function to become unstable because the same objective value can result from a different combination of parameter values. For instance, the parameters σ and λ for $\exp(-(\ldots)^2/\sigma)\exp(-\lambda(\ldots))$ in Equation (11) of the Vogelstein algorithm (Vogelstein et al., 2010) are interacting and can lead to unstable optimization (**Figure 2**). However, our method does not have this problem, because the sub-objective functions, Equations (6, 7) have only one single free parameter each, k_1 and k_2, respectively, as they are optimized alternatingly with respect to $\boldsymbol{n}$ and $\boldsymbol{a}$. Both k_1 and k_2 are determined solely by λ_0.

The same instability occurs with respect to estimating the spatial filter, α, and the estimated calcium trace, **C** (Equations 33 and 36 of Vogelstein et al., 2010). Moreover, the spatial filter α in the Vogelstein algorithm is unconstrained and could be negative, thus potentially yielding erroneous estimates. In contrast, our method constrains the spatial filter **a** to be both non-negative and upper-bounded. This prevents the main objective function from oscillating through alternating optimizations of $\boldsymbol{n}$ and $\boldsymbol{a}$.

Application of our method reliably estimated the actual spike rate (**Figures 2A**left,**C**) and outperformed the Vogelstein algorithm by producing higher correlation (25% higher, $p < 0.05$) to actual spikes simultaneously recorded (**Figure 2C**). Data from an optical-imaging only session also showed reliable results by identifying rapid calcium transients as spikes (**Figure 2B**). In addition, our method shows clear empirical convergence of the learning curves (e.g., **Figures 2A,B**) together with the above theoretical guarantee in accordance with convex optimization theory.

Cell and Neuropil Analysis

To estimate the spike rate, the pre-processed (HPF) fluorescence signal was normalized, pixel by pixel, by calculating $(F - F_0)/F_0$ (i.e., ΔF/F). F_0 was defined as the mean of the fluorescence values that were less than 2 standard deviations above the overall mean for that pixel. This value was chosen to exclude outlier values, which were likely related to spike activity. Spike rates were then estimated by applying the method described above (**Figure 2**) to the pixels constituting a cell body. Following spike train estimation, a threshold of 1/2 × standard deviation of the spike rate was used to suppress spurious spikes arising from photon noise. This threshold was found to work well in that it was less likely to suppress activity generated by actual spikes, because spike-rates were sparse and exponentially distributed and thus had small standard deviations. We tested different thresholds, including zero, and none of them changed the results we present in this paper.

To calculate percent fluorescent change in a cell, the mean ΔF/F was calculated by projecting the ΔF/F matrix (time-point samples × pixels in the cell) onto the spatial filter $\boldsymbol{a}$ (pixels × 1), and normalizing by the sum of the coefficients a_i to produce a weighted mean. The filter α was optimized from the deconvolution algorithm.

Around each cell, a local neuropil patch was defined by selecting an annulus with radii of 7–15 μm centered around the middle of the cell body. Unless explicitly specified, all neuropil results shown in the present study were drawn from this neuropil patch size. We chose the minimum inner radius as 7 μm to minimize contamination from the cell signal onto the neuropil patch. In accordance with a previous report for the size of cell somata in mouse visual cortex (Braitenberg and Shchuz, 1998), this was indeed large enough to exclude any pixels from other cell somata, by visual inspection. Other cell bodies, glia, and dark blood vessel regions were similarly excluded. After the application of HPF (cut-off at 0.05 Hz), the ΔF/F was calculated in single pixels with the same method as for the cell somata, and then averaged across all pixels within the patch.

The mean response to the visual stimulus was calculated for each ROI (cell or neuropil) after subtracting the mean ΔF/F response over the last 3 frames prior to stimulus onset. An aggregate response was computed by averaging the calcium signal over a period corresponding to the duration of the stimulus presentation (600 ms), centered at the peak frame of the mean response computed across the cell population for stimuli at 100 and 40% contrast. This strategy was particularly important for anesthetized animals because the time course of the calcium signal was more prolonged (Haider et al., 2013), peaking near the end of the stimulus presentation. Cells were called visually responsive if they had a significant mean response across all stimuli presented at 100% contrast (i.e., $\Delta F/F > 0.5\%$). For GCaMP6s data, we included cells with mean $\Delta F/F > 5\%$ across stimulus conditions in the analysis. In the analysis that follows we used visually responsive cells and their surround neuropil patches.

Fano factors were calculated from ΔF/F (%) responses individually for the 6 stimulus conditions, and averaged across the two grating orientations presented for each given contrast. Mean Fano factors of cells and neuropil patches, and their ratios ($F_{cell}/F_{neuropil}$), were calculated across each FOV. The overall mean and SEM of the ratio is reported across FOV's. Note that even though Fano factors were calculated here using ΔF/F (%) responses instead of spike rates, they are still useful for comparing the relative variability between cell and neuropil and across different brain states.

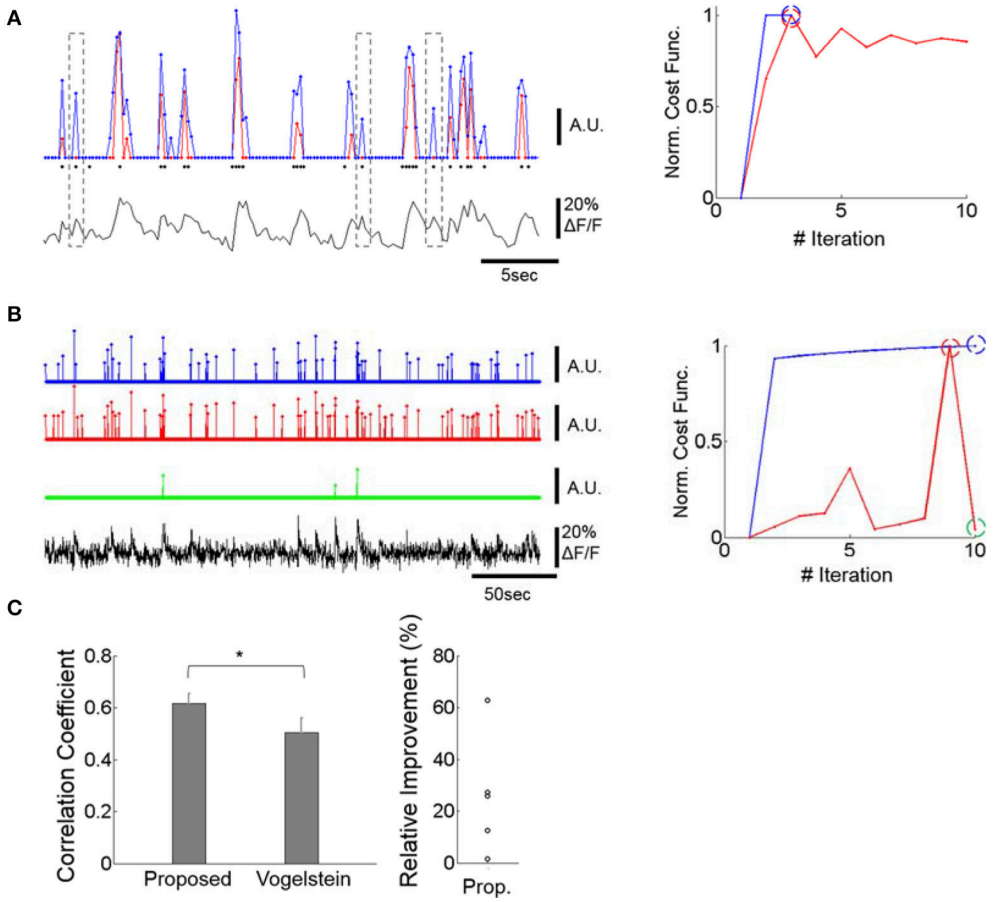

FIGURE 2 | Improving spike inference from the calcium signal. **(A)** Example of spike trains inferred by our deconvolution algorithm and by a previously published method (Vogelstein et al., 2010). Left bottom: OGB calcium fluorescence trace of a cell whose spikes were measured via patch-clamp recording. Left Top: The prediction of our deconvolution method (blue) vs. the Vogelstein method (red, Vogelstein et al., 2010). Actual spike events at the time of image frames are overlaid as black dots. The events do not include the spike numbers. For major calcium transients both methods show similar predictions. For intermediate and low calcium transients, however, our method identifies action potentials with greater sensitivity than the Vogelstein method (see dotted outlines). This is reflected in a higher correlation of the deconvolved to the actual spike rates (0.64 for ours, 0.51 for Vogelstein). Right: Convergence of our method (blue) vs. Vogelstein's method (red) as a function of the number of iterations, applied to the time-series of a cell's calcium signal. Blue and red dashed circles indicate the iteration at which algorithms return the optimal estimates. **(B)** Example of spike trains inferred by the two methods in a typical calcium signal recording. Left: Both methods identify strong calcium transients (blue and red) at the maximum of the cost function within 10 iterations performed. The green graph shows spike identification at an iteration (iteration = 10), where the spike identification is markedly poorer than in iteration nine, where the best result was obtained. For visualization, each estimated spike-rate train was thresholded at 3x standard deviation. Since spike trains are sparse, thresholding did not significantly suppress spike rates. In particular, the green trace was not affected by this thresholding process. Right: Learning curve of the two methods. The blue, red, and green dashed circles indicate the iterations at which the estimates were obtained. While the learning curve of the Vogelstein method does not converge after multiple iterations, the proposed method shows a monotonic increase of the learning curve. This illustrates that the Vogelstein method can be inherently unstable, whereas the method proposed here is stable by converging monotonically. **(C)** Correlation between deconvolution algorithms and actual spike trains for 5 patched and imaged units (left) and relative performance improvement of our method (right). Left: The proposed method shows significantly higher correlation ($p < 0.05$; paired t-test, $n = 5$) than the Vogelstein algorithm. *$p < 0.05$. Right: Each circle represents a relative increase of correlation coefficient, i.e., [Proposed – Vogelstein]/Vogelstein, for each patched cell.

Noise Correlation Analysis

For noise correlation analysis, pairwise Pearson's correlation coefficients between pairs of cells, pairs of neuropil-patches and between cells and neuropil-patches, were calculated for each stimulus condition. Noise correlation coefficients were calculated in a standard fashion, with single trial-responses subtracted from the mean-response across trials within each stimulus condition. Then, noise correlation coefficient values of two directions in each contrast were averaged to obtain a mean noise correlation coefficient at the given contrast. For cells, estimated spike responses (see above) were used to calculate noise correlation coefficients. Since neuropil activity reflects a broad, mixed, aggregate of neural processes including excitatory and inhibitory activity, we have not applied spike estimation to the neuropil signal. Neuropil-to-neuropil and cell-to-cell noise correlations were grouped separately according to their distance and averaged to yield the mean noise correlation coefficient as a function of distance. Linear fits to these plots were obtained per

FOV and used to compare between the linear decays of neuropil-to-neuropil and cell-to-cell noise correlations by performing a statistical test for difference between the two slopes (Cohen, 1975) as follows:

$$\text{Neuropil: } y_{np} = \alpha_{np} x_{np} + \beta_{np},$$
$$\text{Cell: } y_c = \alpha_c x_c + \beta_c,$$

$t = (\alpha_{np} - \alpha_c)/\sqrt{SE^2_{\alpha_{np}} + SE^2_{\alpha_c}}$, where SE indicates the standard error of a slope.

$t \sim T(n_{np} + n_c - 4)$, where T is the t-distribution, and n_{np} *and* n_c are sample numbers of neuropil and cell data, respectively. This slope test was also performed between brain states within either cell or neuropil noise correlation. To avoid local neuropil contamination of cell somata, we restricted the correlation analysis to cell and neuropil patches that were at least 30 μm apart from each other.

We also measured *noise* cross-correlations between the cell soma and a set of adjacent, 2 μm-thick neuropil annuli located at progressively larger distances from the center of the cell soma. Briefly, (1) 2 μm-thick annular neuropil patches whose radii increased incrementally (31–33, 51–53 μm, and so forth) were defined, (2) the mean cross-correlations between the cell soma (spike-estimate) and its corresponding neuropil patches (ΔF/F) were measured across each FOV, and (3) the overall mean and standard error of the mean (SEM) were calculated across all FOV's.

Neuropil Correlation Analysis after Linear Subtraction of Adjacent Cell Response

To estimate the contribution of single cells' responses to neuropil activity, single cells' responses weighted with a common scale value were subtracted from neuropil responses. The common scale value was estimated through a linear regression model: $\boldsymbol{y} = \boldsymbol{X\beta}$, where y is an $n \times 1$ vector composed of n neuropil patch responses, $\mathbf{X}$ is a $n \times 2$ vector composed of an $n \times 1$ vector of cell responses and an $n \times 1$ vector of 1s, $\boldsymbol{\beta}$ is a 2×1 vector, composed of a scale value and a bias. After subtracting cell responses with the common scale value $\boldsymbol{\beta}$, the residual neuropil responses, $\boldsymbol{y_r} = \boldsymbol{y} - \boldsymbol{X\beta}$, were used for correlation analysis to measure the linear subtraction effects. Even though the use of a common scale value across all pairs of cells and adjacent neuropil patches within an FOV does not take into account varying interactions of individual pairs, the overall effects from the linear subtraction can still be assessed under the assumption that overall effects are similar across FOV's and brain states.

Decoding Accuracy of Cell Populations versus Neuropil Patches

To compare the decoding accuracy for direction discrimination between cells and neuropil patches, optimal linear decoding was used (Duda et al., 2001). First, the responses of visually responsive cells to the stimulus were transformed into a vector representing a population rate code in each trial. Then, 10-fold cross-validation tests were performed by leaving out 10% of the data for testing, and training the classifier with the remaining 90%. Discriminability between vertical and horizontal gratings was measured separately for each contrast level.

Decoding accuracies of n-element populations were calculated by selecting n cells or n neuropil patches randomly from each FOV in each trial, collecting their responses into a population vector, calculating the vector's direction decoding accuracy, and averaging decoding accuracies across vectors drawn independently across 1,000 trials. The decoding accuracy in each trial was calculated by averaging 10 decoding accuracy values from 10-fold cross-validation tests. Then, the overall mean and SEM were obtained across FOVs. In this procedure, a smaller neuropil patch size (annulus radii of 7–11 μm) was chosen, which reduced the overlap of pair-wise neuropil patches to <0.5% of the patch area to minimize artificially generated signal correlations.

Neuropil decoding accuracies were also compared across a range of patch sizes: 7–11, 7–50, 7–100, …, 7–250 μm radii. Each patch was centered around the corresponding cell, and thus the overlap ratio between patches increased with patch size. As neuropil patch size increased, some neuropil patches completely overlapped with other patches (i.e., <0.5% for 7–11 μm to >80% for 7–250 μm). Therefore, as optimal linear decoders require full ranks of data, we removed some patches when adding a new patch in the population vector did not increase the rank of data. Again, all decoding accuracies were computed from 10-fold cross-validation tests.

Direction Discriminability within Single Cells and Neuropil-Patches

To assess direction discriminability of cell and neuropil activity, we used d':

$$d' = \frac{\left[mean\left(x^h\right) - mean(x^v)\right]}{\sqrt{0.5\left(var(x^h) + var(x^v)\right)}}$$

where x represents a trial-response of either cell or neuropil-patch conditioned on stimulus direction, which is denoted with superscript v (vertical grating) and h (horizontal grating).

Then, we compared the spatial organization between the d's of cells vs. their local neuropil-patches by calculating a spatial Pearson correlation coefficient between the corresponding d' values, within each FOV. To assess the statistical significance of the spatial correlation, we built a null distribution from correlation coefficient values obtained from 10,000 shuffled datasets. Each shuffled surrogate dataset was generated by randomly shuffling the spatial order of cells, thereby destroying the spatial relationship between cells and neuropil patches. From the null distribution, the statistical significance of the original spatial correlation between cell and neuropil-patch d' values could be assessed.

RESULTS

Visually-Evoked Neuropil Response Strength and Response Reliability

To explore visually evoked neuropil responses, we measured and compared percent fluorescence change (ΔF/F) seen in neuropil-patches vs. cell somata. Both neuropil and cell responses to visual stimulation were strongly modulated compared to baseline activity (i.e., the activity in the absence of visual stimulation), cell responses (ΔF/F) being generally weaker across different contrasts than neuropil responses (**Figure 1D**). Furthermore, the ratio of cell to neuropil-patch response strength decreased with falling contrast (**Figure 1E**), because somatic activity dropped faster than neuropil activity as contrast was lowered. This was true both in the awake state (AW) and under anesthesia (AN) (**Figure 1E**).

As expected, changes in brain state affect both neuropil and somatic responses. Specifically, light (0.7% isoflurane) anesthesia markedly increased visually driven activity in the neuropil (**Figure 1D**) and less so in the L2/3 neurons themselves. As a result, the ratio of visual response strength in L2/3 cells vs. adjacent neuropil patches was lower under light anesthesia than in the quiet awake state (**Figure 1E**).

Response Reliability

We compared the reliability of cell responses to neuropil-patch responses when exposed to the repeated presentation of identical moving grating stimuli. Cell responses were highly variable whereas neuropil responses, even for small patches, showed much greater reliability. We calculated and compared the Fano factors of cells vs. neuropil-patches using the calcium signal [variance/mean calculated using the ΔF/F (%) response; see Section Materials and Methods]. The Fano factors of neuropil annuli (radii 7–15 μm from the cell soma) were 5–20 times smaller than the Fano factor of their corresponding cell ($P < 1e\text{-}8$; the main effect between cell vs. neuropil-patch in two-way ANOVA; **Figure 3A**), reflecting the high reliability of aggregate neuropil responses. This suggests that the high randomness of cell firing results either (i) from the cells' own internal processes, or by (ii) sub-selecting a specific subgroup of inputs with higher variability than seen in the aggregate neuropil activity. Naturally, Fano factors increased as the number of pixels in the neuropil patch decreased, but even small 5-pixel neuropil patches ($\sim 11\ \mu m^2$; covering ∼ 4–7 times smaller area than the cell body) still yielded ∼2 times smaller Fano factors than those of cells (1.86; **Figure 3B**). Mean neuropil Fano factors approached the cellular Fano factors for small (1 pixel = $\sim 2.25\ \mu m^2$) neuropil patch sizes, but then rapidly dropped for patches of bigger sizes (**Figure 3B**).

The relative reliability of neuropil to cell responses varies as a function of visual contrast. Cell-to-neuropil Fano-factor ratios decreased with falling stimulus contrast in L2/3 (1 and 5 pixels, and annulus with 7–15 μm radii; $P < 5e\text{-}4$, in Two-way ANOVA; **Figure 3B**). This suggests that a fraction of the projections included in L2/3 neuropil patches fire less reliably than local L2/3 cells do as contrast decreases. The relative reliability of cell to neuropil responses varied less strongly as a function of brain state. Typically, cell-to-neuropil Fano-factor ratios were slightly higher in the quiet awake compared to the lightly anesthetized state (**Figure 3B**), however significance was not reached ($P > 0.5$ for 1- and 5- pixels, and $P = 0.06$ for annulus radii with 7–15 μm in Wilcoxon rank-sum test), suggesting that changes in brain state may affect more uniformly the local and non-local neural processes that constitute the L2/3 neuropil patches examined.

In summary, we found that visually evoked responses of both cells and adjacent neuropil patches depend on brain state, and that the ratio of cell to neuropil response magnitude is much larger during quiet wakefulness than under light anesthesia. Neuropil patch responses to drifting gratings were always more reliable than L2/3 cell responses, setting a limit on the degree to which the spatially coherent signal carried by the neuropil, which may arise as a projection from other areas, can fluctuate randomly from trial to trial. Furthermore, neuropil activity does not simply reflect the linear sum of nearby cell activity since cell-to-neuropil fano-factor-ratios change as a function of visual contrast.

Neuropil-to-Neuropil, Cell-to-Neuropil, and Cell-to-Cell Noise Correlations

Noise correlation analysis is thought to provide information about the spatial organization of shared "internal" input modulations due to brain state fluctuations (Niell and Stryker, 2010; Ecker et al., 2014) and other global modulatory inputs (Polack et al., 2013) that influence neuronal activity. Noise correlations between different disjoint neuropil patches, measured from ΔF/F responses, were high (∼0.82 under light anesthesia vs. ∼0.67 in quiet wakefulness, $P < 1e\text{-}8$, Wilcoxon rank-sum test; **Figure 4A**, Left), in line with prior observations that demonstrated the high spatial coherence of the neuropil signal (Kerr et al., 2005). Notably, these values are strikingly different from the strength of cell-to-cell noise correlation coefficients, which were much lower (<0.1 in anesthetized, ∼0.05 in the awake state; **Figure 4A**, Right). Note that this pattern was preserved even when calculating cell correlations using ΔF/F responses rather than the extracted spikes (Supplementary Figure 3). This is expected since the inter-stimulus-interval chosen was longer than the typical temporal decay (i.e., $\tau = \sim 1$ s) of OGB events. One possible explanation for this difference is that a local volume of neuropil integrates numerous synaptic processes (Braitenberg and Shchuz, 1998; Chklovskii et al., 2002) that may extend over considerable cortical distances, providing the same signal to different neuropil patches. The spatially coherent part of this signal may not modulate individual units strongly. Alternatively, the aggregate activity of neuropil processes may contain a spatially coherent signal, which is filtered out in pairwise cellular noise correlations by the stochastic firing of individual units.

Despite the high spatial coherence of neuropil activity, neuropil-patch to neuropil-patch noise correlation strength decayed substantially as a function of cortical distance regardless of brain state (**Figure 4A**). For example, neuropil patches <60 μm apart from each other had significantly stronger noise correlations compared to patches located 180–210 μm from each

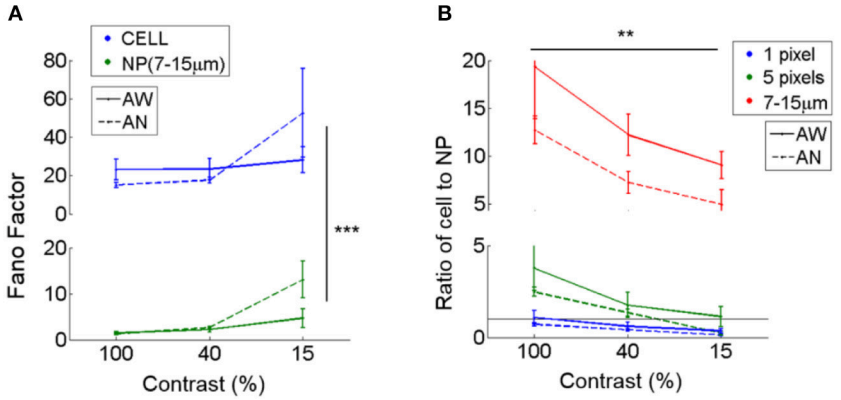

FIGURE 3 | Fano factors of cells vs. adjacent neuropil patches. Fano factors (variance/mean) were estimated in cells and nearby surrounding neuropil patches. Fano factors were calculated based on ΔF/F responses, and thus the absolute scale is different from that calculated using spike rates measured by electrophysiology. **(A)** Mean Fano factor across cells (CELL) vs. adjacent annular neuropil patches (NP; radius 7–15 μm). Neuropil patches show smaller Fano factors (1.4–2.4 at 100 and 40% contrast; 4.7–13 at 15% contrast) across all brain states and visual contrasts compared to cells (15–23 at 100 and 40% contrast; 28–52 at 15% contrast), suggesting that 7–15 μm neuropil-patch responses to repetitions of identical stimuli are much less variable than cellular responses. ***Denotes a significance level of $P < 1e\text{-}8$ in comparison between Fano factors of cells and neuropil-patches (Two-way ANOVA). **(B)** Ratio of the mean Fano factor across cells vs. across neuropil patches. Neuropil patches of different sizes are illustrated in different colors. Neuropil patches with 1 or 5 pixels were defined by randomly selecting 1 or 5 pixels within annular neuropil patches centered around the cell extending from 7 to 10 μm. A ratio of 1 is shown as a black horizontal line. Mean neuropil Fano factors approach the cellular Fano factors for small (1 pixel = ~2.25 μm^2) neuropil patch sizes, but then rapidly drop for patches of bigger sizes. **Indicates a significance level of $P < 5e\text{-}4$ across contrasts (Two-way ANOVA).

other (9 and 15% decrease for the anesthetized, awake state, respectively; $p < 0.05$, *one-tailed Welch's t*-test; **Figure 4A**, Left). This was true both in quiet wakefulness and under light anesthesia. In contrast to neuropil inter-patch noise correlations (**Figure 4A**, Left), pairwise cell noise correlations were flatter as a function of distance (slopes significantly different at $P < 0.05$ for both brain states, *t*-test for two slopes; **Figure 4A**, Right), decreasing more slowly with increasing distances (Kerr et al., 2007; Smith and Kohn, 2008; Golshani et al., 2009; Rothschild et al., 2010; Denman and Contreras, 2013). Nonetheless, because they start at a much lower value, the relative decrease of cell-to-cell noise correlation strength was larger for the same cortical distance (i.e., <60 vs. 180–210 μm), decreasing by 29 and 18% for the anesthetized, awake, state, respectively (**Figure 4A**). This may potentially reflect a difference in the spatial organization of neuropil processes, largely reflecting synaptic activity, vs. the spatial organization of L2/3 cellular activity. Certainly, the large spatially coherent component that imparts to the neuropil its high noise correlation strength appears to be largely filtered out in L2/3 cell output activity.

Note that, since noise correlation strength for pairs of cells is generally close to zero, we further tested whether noise correlation values found in our study are higher than controls, i.e., noise correlation values estimated from shuffling trials randomly for each cell separately within each stimulus condition. This confirmed that, though low, the cell-to-cell noise correlation values we estimated are highly significant (i.e., Supplementary Figure 4).

To further explore how cell responses are related to neuropil responses, we measured *noise* cross-correlations between cells and a series of annular neuropil patches centered at increasing distances from the cell soma. Patches were chosen to be 2 μm-thick annuli located at progressively larger distances from the cell center. Neuropil-to-cell cross-correlation coefficients were compared to cell-to-cell cross-correlation coefficients. Pairwise cell-to-cell noise correlation coefficients were calculated using spike rates estimated from the calcium signal (see Section Materials and Methods and **Figure 2**). Neuropil-to-cell noise correlations were markedly lower than neuropil-patch to neuropil-patch ones, but still larger than cell-to-cell noise correlations ($P < 1e\text{-}30$, Wilcoxon rank-sum test; **Figure 4B**). This suggests that neurons efficiently filter out the major part of the highly coherent, spatially uniform, neuropil modulation component. We also found that coherence between cell and neuropil responses is brain state-dependent, yielding significantly lower noise correlation coefficients in the quiet awake state vs. under light anesthesia ($P < 1e\text{-}7$, Wilcoxon rank-sum test; **Figure 4B**). This suggests a more heterogeneous activity structure in the quiet awake state.

In summary, neuropil activity exhibits much stronger spatial coherence than cell activity during the repeated presentation of identical stimuli, at least up to distances of ~200 μm and likely higher. The relative decrease of noise correlation coefficient strength as a function of distance is smaller in neuropil than in cells, and both cell and neuropil noise correlation coefficients depend on brain state, being smaller in quiet wakefulness vs. light anesthesia. These observations suggest that L2/3 neurons are capable of filtering out the main, highly coherent, spatially uniform, neuropil modulation component, and that neuropil activity exhibits a more heterogeneous structure in the quiet awake state.

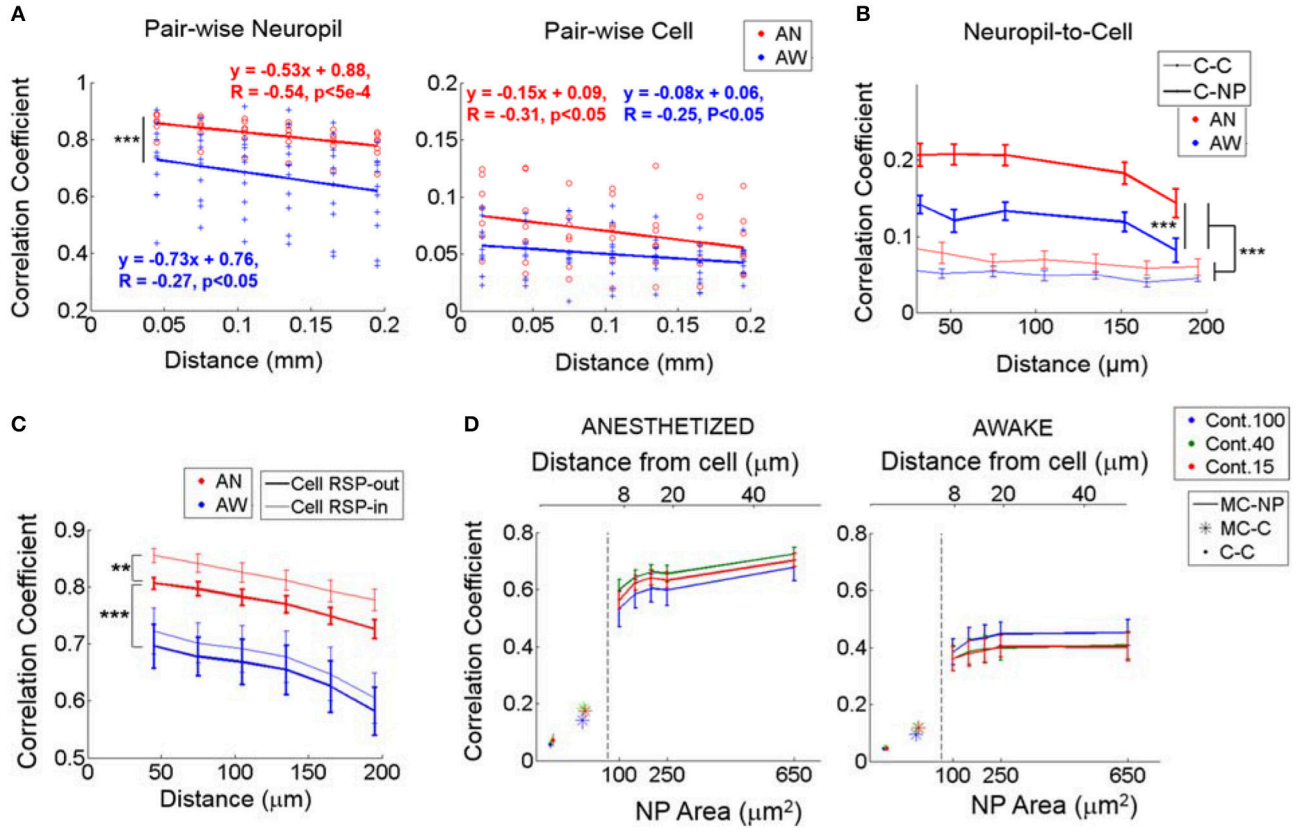

FIGURE 4 | Noise correlations during identical visual stimulation. **(A)** Noise correlation between neuropil-patches (left; from ΔF/F response) and between cells (right; from estimated spikes) as a function of distance. In **(A)**, each value marked with either a red circle (anesthetized) or a blue cross (awake) represent the mean correlation across all pairs belonging to the corresponding distance bin within an FOV. Bin size = 30 μm. While neuropil coefficients decay at a steeper slope than cell coefficients, ($P < 0.05$, *t*-test for the two independent slopes), regardless of brain state, the relative (%) decrease over the same distance is ∼2 times larger for cells (∼23% for cells vs. ∼12% for neuropil patches). **(B)** Noise correlation between neuropil-patches (from ΔF/F response) and cells (from estimated spikes) as a function of distance (bold line, C-NP). "C-C" refers to pairwise cell-to-cell noise correlations. Error bars indicate mean ± SEM at distances used across FOVs. For **(A,B)**, ***indicates $P <$ 1e-7 in Wilcoxon rank-sum test. **(C)** Linear contribution of single-cell response to neuropil-patch noise correlation. Mean noise correlations between neuropil patches were compared before and after subtracting corresponding single cells' responses (see Section Materials and Methods). **, ***$P <$ 5e-5, $P <$ 1e-8, Wilcoxon rank-sum test. "Cell RSP-in": without linear subtraction. "Cell RSP-out": after linear subtraction. Our basic observations remain unchanged after this correction. **(D)** Mean noise correlations between individual cells (C-C), between single cells and the mean response from all other cells except the cell itself (MC), and between the mean cell response (MC) and neuropil patches (NP) as a function of neuropil patch size and its distance from the centered cell. "X-Y", represents noise correlation between "X" and "Y"; for example, MC-NP, correlation between MC and NP. AN, Anesthesia, AW, Quiet wakefulness. Cont.: Visual contrast. Cell responses were measured from deconvolved spike rates. In plots, solid line (with error bar) represents the mean (with SEM) across FOV's ($n = 7$ and 11 from anesthetized and awake animals, respectively).

Contribution of Cell Responses to Nearby Neuropil Activity

To investigate the influence of the activity of individual cells on nearby neuropil activity, we subtracted somatic responses weighted with a common scale value from the adjacent neuropil-patch responses (annulus from 7 to 15 μm centered around the cell). The scale value was simply estimated across all cell-neuropil-patch pairs using a linear regression model between a dependent variable (i.e., the neuropil response) and a regressor (i.e., the corresponding cell response, see Section Materials and Methods for details). Then, we recalculated the noise correlations between neuropil patches. This approach removed the mean linear contribution of individual cells to neuropil activity and allowed us to determine to what degree the spatial structure of neuropil activity described in the previous section could have its origin in the activity of adjacent cells, as might occur, for example, via the back-propagation of action potentials through the cells' own dendritic branches (Waters et al., 2003).

We found that subtracting somatic responses significantly reduced neuropil inter-patch noise correlations only under anesthesia (0.046 vs. 0.023, $P <$ 5e-5 vs. $P =$ 0.24, Wilcoxon rank-sum test), without significantly affecting their profile over distance ($P <$ 1e-8, Wilcoxon rank-sum test between the two brain-states; **Figure 4C**). This is consistent with the observation that single cells are more strongly synchronized with surrounding cell populations and neuropil under anesthesia than in the quiet awake state (Ecker et al., 2014).

Figure 4B shows that neuropil-to-cell noise correlations were considerably stronger than mean cell-to-cell noise correlations, across all distances measured (e.g., 0.18 vs. 0.06 under anesthesia and 0.12 vs. 0.04 for the quiet awake state, respectively, at 150 μm). The high correlation values imply that neuropil patches carry a substantial signal that is correlated with cell activity, even for cells that are quite distant from the location of the neuropil patch (∼150 μm). Although, this might initially appear counterintuitive, it may have an obvious reason: neuropil responses reflect aggregate synaptic activity and are more correlated with mean cell population activity than with individual cell activity. Noise correlation coefficients between individual cell responses and mean population responses were also much higher than the average of all pairwise cell-to-cell noise correlation coefficients. The reason is that the firing of individual cells is stochastic, which disproportionately lowers pairwise cell-to-cell noise correlation coefficients. To test this reasoning, we measured (1) the correlation coefficient between the response of individual cells and the mean cell response (MC) from all other cells except the cell itself (MC-C), and (2) the correlation coefficient between MC and individual neuropil patch responses (MC-NP). As predicted, MC-C noise correlation coefficients were higher than mean pairwise cell-to-cell noise correlation coefficients, and MC-NP correlation coefficients were even higher (**Figure 4D**).

Noise correlations were affected by brain state, being generally higher during anesthesia (**Figure 4D**, compare left to right plot). This was particularly true for the MC-NP cross-correlation values, which were 80% higher under anesthesia (0.74 at 50 μm) vs. in the quiet awake state (0.41 at 50 μm; **Figure 4D**). It is therefore likely that under anesthesia, the population of cells is strongly driven by the activity of shared inputs. It is also likely that in the quiet awake state, sparse and more localized patterns of firing activity are predominant (Greenberg et al., 2008; Sawinski et al., 2009), leading to smaller noise correlation coefficients.

In summary, removing the neighboring cell calcium signal component from the neuropil signal does not change the spatial profile of the neuropil-to-neuropil noise correlation structure. Furthermore, cell to neuropil-patch noise correlations are significantly stronger than the mean cell-to-cell noise correlation. This is likely due to the stochastic nature of cell firing, which disproportionately lowers pairwise cell-to-cell noise correlation coefficients.

Decoding Direction Information from Neuropil Patch Populations

Mice lack orientation columns and are thought to have a salt and pepper pattern of orientation/direction preference (Ohki et al., 2005). However, a recent study suggests that orientation preference may not be entirely randomly distributed across neurons, as neighboring cells show greater similarity in orientation preference (Ringach et al., 2016). Neuropil neighborhoods of appreciable size contain numerous cell processes. Assuming orientation/direction preference is randomly distributed across these processes, neuropil-patches surrounding neurons should show little, if any, orientation/direction bias. Alternatively, neuropil processes may be organized in regions with coherent orientation/direction preference, which changes gradually along the cortical surface. In what follows we ask whether neuropil activity conveys sufficient information to decode visual direction and how this compares to the direction discrimination accuracy of nearby cell populations (see Section Materials and Methods).

We find that populations of neuropil-patches show high decoding performance, commensurate with that of populations of neighboring neurons (**Figure 5A**, Left), both in quiet wakefulness and under light anesthesia. This high decoding performance from neuropil-patch populations did not result just from differences in the global modulation of aggregate neuropil activity depending on stimulus direction since direction selective information is essentially lost and discrimination accuracy drops to chance levels when we average over all neuropil patches within an FOV (**Figure 5A**, Right). It also did not result from the "contamination" of neuropil activity by adjacent cell signals, since the linear subtraction of cell signals from adjacent neuropil-patch signals did not change decoding performance (Supplementary Figure 5A). Finally, the similar performance between cell and neuropil-patch population was not due to an underestimation of cell decoding performance due to inappropriate processing of cell data. Correcting the cell signal for neuropil contamination with correction factor (S) within the empirically determined range ($S = 0.4$–0.6) increased, rather than decreased, the decoding performance of the cell population, particularly at 100% contrast (Supplementary Figure 5B). The decoding performance also increased when estimated spike data from the cell calcium signal were used, rather than the calcium signal (i.e., $\Delta F/F$ response) itself (Supplementary Figure 5C).

To better understand the sources of high neuropil decoding performance, we assessed whether the spatial organization of neuropil patches for stimulus encoding is correlated with those of adjacent cells. To this end, we first calculated the extent of discriminability between the two stimulus directions, called *d'*, for single cells and neuropil-patches, respectively (see Section Materials and Methods). Then, we calculated a spatial Pearson correlation coefficient between the *d'* values of cells and their local neuropil-patches within each FOV and compared it with a null distribution generated from surrogate data, where the cells' spatial locations were randomly shuffled (see Section Materials and Methods). This test showed that neuropil activity was correlated with adjacent cell activity in terms of spatial organization relevant to stimulus encoding (**Figure 5C**). In particular, significance was only reached in the quiet awake state (**Figure 5C**, Right). Nonetheless, the magnitude of this correlation was not sufficient to explain the high neuropil decoding performance, particularly in the anesthetized state, in which the absolute correlation coefficient among *d'* values was weak and not significant (**Figure 5C**, Left). To further investigate the reason for the high decoding performance of neuropil activity, we measured the mean and variance of cell and neuropil-patch *d'* values within each FOV. On average, *d'* variances were significantly smaller, and mean absolute *d'* values were significantly larger across neuropil-patches compared to cells (**Figure 5B**). Therefore, in terms of the capacity for information encoding, neuropil activity shows higher and more

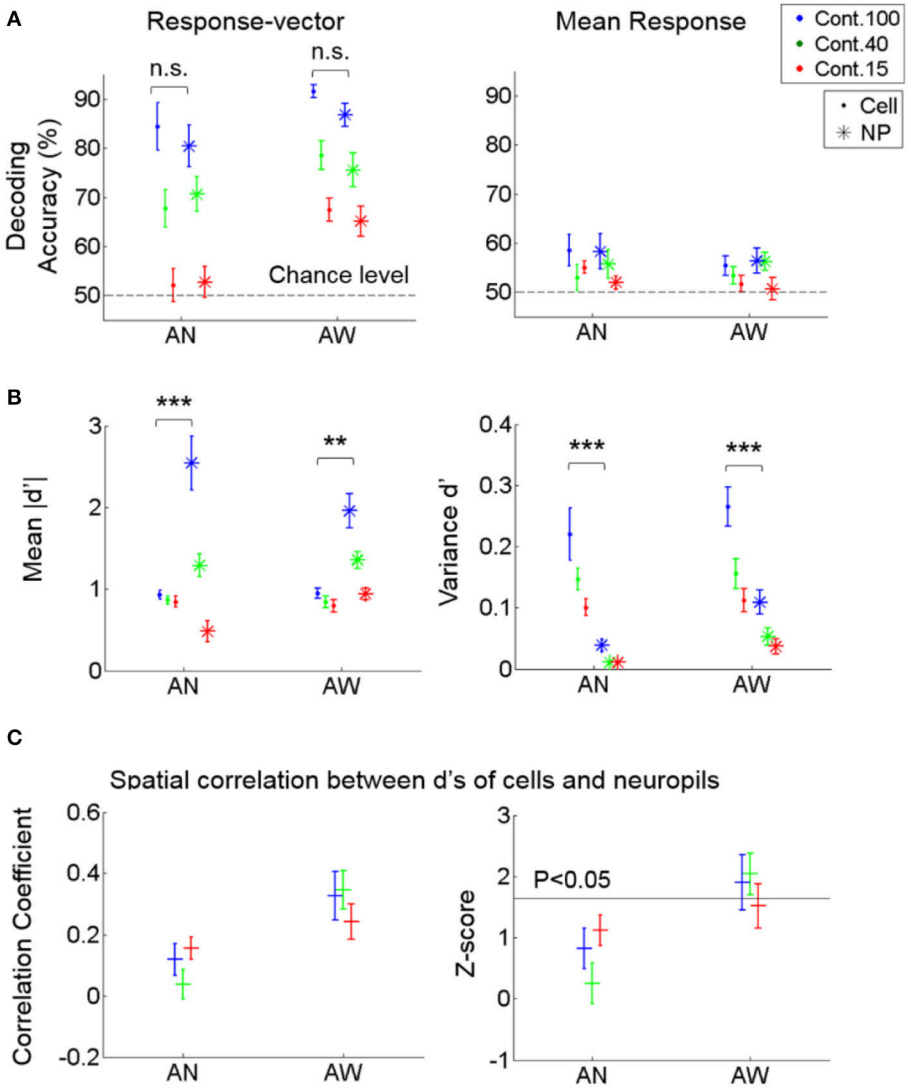

FIGURE 5 | Decoding performance of cell vs. neuropil responses for stimulus direction. **(A)** Decoding accuracy from response vectors composed of cells vs. neuropil-patches (left) and from the mean response across cells vs. neuropil-patches within FOV's (right). Decoding accuracy was not significantly different for neuropil-patch vs. somatic response-vectors regardless of brain state (not significant in Two-way ANOVA). Response-averaging across population elements dropped the decoding performance to near chance level for both cells and neuropil patches. **(B)** Mean of absolute d' values (left) and variance of d' values (right) within each FOV, averaged across FOV's. d': discriminability between vertical vs. horizontal grating conditions for single cell or neuropil-patches. On average, while the mean of absolute d' values within an FOV is larger for neuropil-patches than for cells, the variance of d' values is smaller across neuropil-patches. **, ***$P < 5e\text{-}4, 1e\text{-}7$ in Two-way ANOVA. **(C)** Spatial correlation between the d's of cells vs. their local neuropil-patches (left) and the corresponding z-score (right; see Section Materials and Methods). Cell and neuropil patch *d'* vectors are significantly spatially correlated only in the quiet awake state ($P < 0.05$). In all plots, "." stands for cell, "*" for neuropil, "+" represent the overall mean across FOVs, and error bars SEM across FOVs ($n = 7, 11$ for anesthetized and awake animals). AN, Anesthesia, AW, Quiet wakefulness.

spatially uniform discriminability between the chosen stimulus conditions than cell activity.

We also examined how direction discrimination accuracy varies as a function of population-vector size and as a function of neuropil patch size. As expected, we found that including more cells or neuropil-patches increased decoding accuracy for both cell and neuropil-patch populations (**Figure 6A**). Interestingly, cell and neuropil-patch populations showed similar accuracy in decoding the (coarse) grating drifting-direction difference we tested across all population sizes tested. Neuropil-population decoding accuracy decreased as neuropil patch size increased (**Figure 6B**). However, regardless of brain state, the decay was slow, and high direction discrimination accuracies (e.g., ∼75% at 100% contrast) were still present for patches with radii as large as 250 μm. This high decoding accuracy was not directly related with distance between cells and between neuropil-patches for at least $n = 4$ within 200 × 200 μm (Supplementary Figure 6). This suggests that, due to the high response reliability of the neuropil,

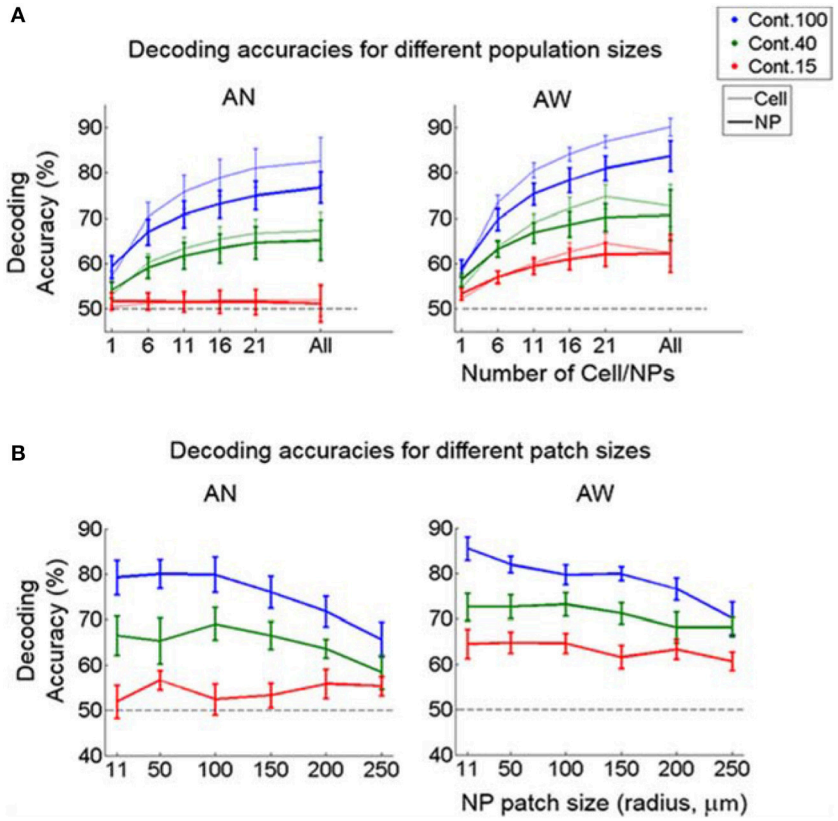

FIGURE 6 | Decoding accuracy as a function of population-vector and neuropil-patch size. **(A)** Decoding accuracy as a function of population-vector size. Decoding accuracy of both cell and neuropil-patch populations increase in a similar way as a function of population-vector size. Decoding accuracies of the neuropil population are slightly lower for $n > 6$, but this does not reach significance on the F-test. **(B)** Decoding accuracy as a function of neuropil patch size increases by enlarging the outer annulus radius, while keeping the inner radius constant at 7 μm. Note that decoding accuracy remains high well beyond neuropil patches with radius ∼100 μm. Blue: 100%, green: 40%, red: 15%. Error bars represent SEM across FOV's. AN, Anesthetized state; AW, Awake state. Dashed lines represent the chance level of accuracy.

even a small amount of spatial inhomogeneity is enough to accurately decode the direction difference employed.

Finally, our results are not a byproduct of using OGB but extend to the GCaMP class of calcium indicators. Specifically, we repeated our analysis in area V1 of mice expressing GCaMP6s genetically. The results were entirely consistent with the analysis of the OGB signal (**Figure 7**), increasing confidence in our findings.

DISCUSSION

We explored the properties of visually driven neuropil activity recorded in L2/3 of mouse area V1, how it relates to the activity of neighboring cells, and whether it can be effectively decoded to perform coarse stimulus orientation discrimination.

Cell vs. Neuropil Visual Response Strength and Reliability

The neuropil in layer 2/3 of mouse primary visual cortex (V1) showed strong visually evoked responses both under anesthesia and during quiet wakefulness. Neuropil ΔF/F responses were in fact stronger, on average, than cell ΔF/F responses at all contrasts (**Figure 1**). The ratio of neuronal to nearby neuropil ΔF/F responses depended on brain state. Specifically, this ratio was lower in the anesthetized compared to the awake state (**Figure 1E**) suggesting that synaptic processing is less efficient under anesthesia. Interestingly, the ratio of neuronal to neuropil response strength was higher for high contrast stimuli irrespective of brain state (**Figures 1D,E**). This also suggests higher efficiency in synaptic processing at higher contrasts.

Neuropil patch responses were always considerably more reliable than local L2/3 cell responses. This result may be thought of as largely expected, since a neuropil patch represents aggregate activity originating from the processes of many cells (see **Figure 3**). However, it is not altogether trivial, since it sets a limit on the degree to which the spatially coherent signal carried by the neuropil (which might arise as a result of input from other areas or subcortical structures) fluctuates randomly from trial to trial. The higher Fano factor seen in cell responses may result from the cell's own internal nonlinear processing from sub-threshold activity to spike output. For example, this elevated randomness in cell firing may be related

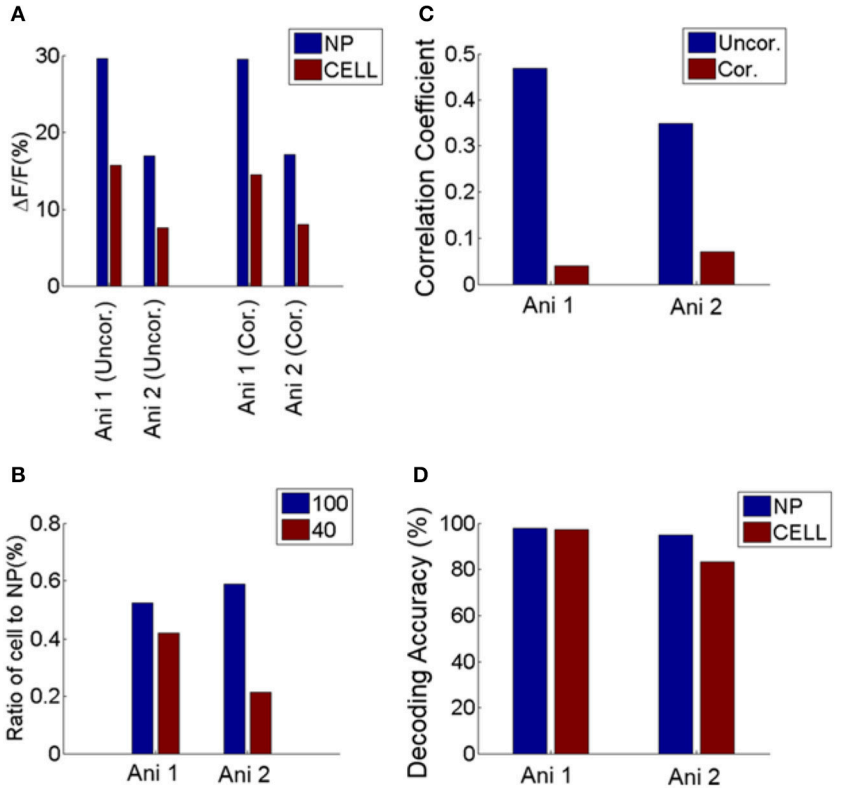

FIGURE 7 | Comparison between neuropil and cell responses from two GCaMP6 expressing animals. **(A)** Mean response of cells and neuropil-patches to 100% and 40% contrast. This is comparable to **Figure 1D**, obtained with OGB. **(B)** Ratio of mean somatic vs. mean neuropil responses at 100 and 40% contrast. These ratios are plotted after correcting for neuropil contamination, and are comparable to **Figure 1E**. **(C)** Decrease of noise correlation coefficients after contamination correction with $S = 0.6$, comparable to Supplementary Figure 2. **(D)** Decoding performance of cell and neuropil-patch response vector for stimulus direction (0 vs. 90°). Decoding accuracy was computed within each contrast condition and averaged across 100% and 40% contrasts. Both datasets showed high decoding accuracy for both neuropil-patch and cell population vectors. Decoding accuracy for GCaMP6s data was obtained with n (population vector size) = 100 for Animal 1 (Ani. 1) and 44 for Animal 2 (Ani. 2). These plots demonstrate that our findings are consistent across both OGB and GCaMP experiments. Note that during this experiment the animal was sedated (see Section Materials and Methods).

with the mechanism known as "iceberg effect," which refers to increased variability in cellular firing that occurs when the firing threshold approaches the peak of stimulus-elicited membrane potential fluctuations (Priebe and Ferster, 2008). Alternatively, cells may sub-select a particular combination of inputs, that displays high variability. For example, sub-threshold activity reflects the difference between excitatory and inhibitory inputs. This difference, particularly after thresholding, might well be less reliable than the aggregate neuropil activity (which reflects the sum rather than the difference between inhibitory and excitatory inputs).

Fano factors in both neurons and neuropil-patches decrease at higher contrast (**Figure 3A**). However, the relative response variability of cells vs. neuropil-patches, quantified by the Fano factor ratio, increases at higher contrast (see **Figure 3B**). The relative increase of cell response variability at higher contrasts may reflect contrast dependent variability in signal integration and spiking processes internal to the neuron (e.g., contrast-dependent iceberg effect; Priebe and Ferster, 2008) or heterogeneous gain control modulation across different types of internal processes that provide input to the neuron. In contrast, a change of brain-state from quiet wakefulness to light anesthesia appears to have less influence over the cell-to-neuropil Fano factor ratio (no significant increase of the ratio in the quiet awake state compared to under light anesthesia; **Figure 3**). This suggests that brain-state changes explored here modulate the relative reliability of cell to neuropil visual responses less strongly than changes in visual contrast.

In summary, the neuropil shows strong visually evoked responses that depend both on brain state and visual contrast. Visual responses of neuropil patches with an area $>11\,\mu m^2$ (i.e., at least 1/5 the area of a cell soma) were considerably more reliable than cell responses. This suggests that the change in neuronal response variability as a function of visual contrast may be mediated in part by stochasticity in the cell's own nonlinear processing. Alternatively, cells may sub-select a particular group of inputs, or difference between inputs, that displays higher variability.

Noise Correlations of Neuropil vs. Cell Responses

Noise correlations reflect the co-modulation of responses by internal, common, inputs (Bryant et al., 1973; Shadlen and Newsome, 1998; Ecker et al., 2010, 2014). Neuropil-to-neuropil noise correlations were overall very large (i.e., 0.6–0.85) even when neuropil patches were almost 200 μm apart from one another (see **Figure 4A**). Assuming that both neuropil and local field potential (LFP) reflect the aggregate synaptic activity, this strong pair-wise neuropil correlation may be closely related to high correlation in gamma activity of the LFP, which is >0.5 and decreases with increasing distance between electrodes (Ray and Maunsell, 2010).

In contrast, neuron-to-neuron pairwise noise correlations were much lower (see **Figures 4B,C**). The spatial profile of neuropil noise-correlated activity decayed linearly, dropping by ∼11% by ∼200 μm, ∼2 times less than cell-to-cell noise correlated activity, which fell by ∼20% (**Figure 4A**) over the same distance. Noise correlation profiles were brain-state dependent, showing higher correlation coefficients under light anesthesia vs. quiet wakefulness, in agreement with (Ecker et al., 2014). Brain-state dependent changes in noise correlation strength were similar for noise correlations between neuropil-patches, pairs of neurons, or between neurons and neuropil-patches. Notably, these results remained valid even after subtracting the response profile of single cells from the response profile of nearby neuropil patches (**Figure 4C**), suggesting that local neuronal activity (or possibly signal contamination from local neuronal somata) is not the main cause of our observations.

In agreement with (Ecker et al., 2010, 2014), noise correlation strength between pairs of neurons was extremely low, though significantly different from zero (Supplementary Figure 4B). However, neuropil-to-cell noise correlations were significantly higher than the mean pairwise cell correlation for a range of cortical distances from 50 to 150 μm regardless of brain state (**Figure 4B**). The high correlation between cell activity and neuropil signal is reminiscent of the electrophysiology results showing strong correlation between cell and LFP activity (Ray and Maunsell, 2010). Interestingly, they report that the strength of this correlation decreases with distance over a scale of millimeters. In contrast, the correlation remains essentially flat over the much smaller scale (∼200 μm) we examined here. Furthermore, Kerr et al. (2005) argued that spontaneous neuropil modulations seen with OGB mostly reflect signals arising from presynaptic axonal activity. Assuming this is correct, this implies that high spatial coherence in the neuropil reflects inputs shared across cells.

This shared component is also captured by the mean activity across all cell somata (MC) in the FOV (**Figure 4D**). However, because individual cells fire stochastically, pair wise inter-neuronal correlations weaken, resulting in the following relationships: NP-MC > MC-C ∼ NP-C >> C-C (**Figure 4D**). The fact that individual cells are strongly correlated to mean cell activity suggests that, at least up to distances of ∼200 μm, they do receive a substantial amount of shared internal input. This finding is supported by recent studies showing that single cell activity is coupled to population activity (Okun et al., 2015). In addition, we find the stronger correlation between single cell and mean cell activity found under light anesthesia (**Figure 4**) consistent with prior results suggesting that stronger co-modulation occurs across cells during anesthesia vs. quiet wakefulness (Ecker et al., 2014).

In summary: (1) Neuropil activity in mouse V1 is highly correlated over large cortical distances. (2) This large spatially coherent component is predominantly but not completely filtered out in L2/3 cell output activity (**Figure 4**). (3) This is reflected in the fact that single-cell to neuropil-patch noise correlation coefficient strength, though much lower than neuropil-patch to neuropil-patch noise correlation coefficient strength, remains flat as a function of distance across >150 μm (**Figure 4B**). (4) The stochasticity and sparseness of cell firing is likely responsible for the much lower cell-to-cell noise correlation coefficient strength (**Figure 4B**). (5) Both neuropil and cell noise correlation coefficients decrease in quiet wakefulness. Finally, (6) the spatial profile of neuropil noise correlations, which likely reflects primarily the coherence of L2/3 synaptic activity, decays slowly over distance.

Direction Discrimination from Neuropil Activity

Visually driven neuropil responses are both strong and reliable, suggesting that they contain significant information about visual stimulus contrast. It is an open question whether they also contain significant information about stimulus orientation/direction. We found that populations of neuropil patches ranging in size from ∼220 μm^2 (radius ∼8.4 μm) to ∼200,000 μm^2 (radius ∼250 μm) discriminated moving grating direction of motion accurately, on par with corresponding cell populations (**Figures 5**, **6**).

The high neuropil decoding performance was not due to trivial contamination of the calcium signal by nearby cell activity because: (1) the choice of neuropil patch inner diameter (>7 μm radius from the cell center) carefully excluded the region of optical contamination in the X-Y plane, (2) there was, at best, a weak correlation in discriminating power (d') between cells and nearby neuropil patches (**Figure 5C**), and (3) decoding performance remained high even for larger (>100 μm in radius; **Figure 6B**) patches, which aggregate multiple processes with "salt & pepper" direction organization (Ohki et al., 2005). Rather, the high decoding performance of neuropil activity was related to the high neuropil response reliability and corresponding increased sensitivity to spatially distributed information, i.e., high d' values (**Figure 5B**).

A potential caveat is that we computed neuropil discrimination accuracies for two orthogonal directions, and it is not clear how the observed discrimination performance would translate to stimuli that differ by smaller orientation/direction angles. Nonetheless, we provided clear evidence that neuropil patches do encode sufficient direction information to distinguish between two coarse (90° difference) directions (**Figure 5**). Interestingly, the high decoding accuracy of neuropil-patch populations are maintained even if we select patches of relatively

large size (>100 μm in radius), which reflect the aggregate activity of a multitude of neuronal processes (**Figure 6B**).

Technical Implications of Neuropil Contamination Correction

The empirical estimates of the contamination correction factor from neuropil to cell ranged from [0.5 to 0.6] for OGB. In our hands, correcting with this factor was sufficient to correct for the variability in the optical quality of the window. In addition, even though GCaMP6s expressing cells have even larger correlation coefficients than cells labeled with OGB [∼0.3–0.5 (**Figure 7C**) vs. ∼0.2 (Supplementary Figure 2)] before neuropil contamination correction, application of $S = 0.6$, which was not optimized for GCaMP6s data but selected for comparison with OGB, resulted in a similar noise correlation coefficient (i.e., ∼0.05). These observations strongly suggest the necessity of correcting for neuropil contamination before cell noise correlation analysis. Particularly, this would be important for functional connectivity analysis, in which Pearson correlation coefficient is typically used.

CONCLUSIONS

Neuropil responses to visual stimuli (moving gratings) in layer 2/3 of mouse V1 are more reliable and more strongly modulated than somatic responses. Stimulus independent fluctuations in neuropil activity are strong and highly correlated across the cortical surface up to distances of at least 200 μm. This contrasts with cell-to-cell pairwise noise correlations, which are much weaker. Finally, despite the "salt & pepper" organization of orientation preference across V1 neurons (Ohki et al., 2005), neuropil-patch populations show high accuracy for performing coarse direction discrimination, commensurate to the accuracy of corresponding cell populations. This remains true even for patches of radius >100 μm. These observations underscore the dynamic nature and functional organization of the layer 2/3 neuropil signal.

AUTHOR CONTRIBUTIONS

SL and SS conceived the projects. JM, SL, and JP performed experiments. SL developed the new spike estimation algorithm and analyzed the data. SL, SS, and JM wrote the manuscript. SS supervised the project.

FUNDING

This work was supported by a Simons Foundation Pilot Award and R21 NS088457 from NINDS to SS.

ACKNOWLEDGMENTS

The authors thank Dimitri Yatsenko for help generating the bead sample.

SUPPLEMENTARY MATERIAL

The Supplementary Material for this article can be found online at: http://journal.frontiersin.org/article/10.3389/fncir.2017.00050/full#supplementary-material

REFERENCES

Bonin, V., Histed, M. H., Yurgenson, S., and Reid, R. C. (2011). Local diversity and fine-scale organization of receptive fields in mouse visual cortex. *J. Neurosci.* 31, 18506–18521. doi: 10.1523/JNEUROSCI.2974-11.2011

Boyd, S. P., and Vandenberghe, L. (2004). *Convex Optimization*. Cambridge, UK; New York, NY: Cambridge University Press.

Brainard, D. H. (1997). The psychophysics toolbox. *Spat. Vis.* 10, 433–436. doi: 10.1163/156856897X00357

Braitenberg, V., and Shchuz, A. (1998). *Cortex: Statistics and Geometry of Neuronal Connectivity*. Berlin: Springer-Verlag.

Bryant, H. L. Jr., Marcos, A. R., and Segundo, J. P. (1973). Correlations of neuronal spike discharges produced by monosynaptic connections and by common inputs. *J. Neurophysiol.* 36, 205–225.

Chen, T. W., Wardill, T. J., Sun, Y., Pulver, S. R., Renninger, S. L., Baohan, A., et al. (2013). Ultrasensitive fluorescent proteins for imaging neuronal activity. *Nature* 499, 295–300. doi: 10.1038/nature12354

Chklovskii, D. B., Schikorski, T., and Stevens, C. F. (2002). Wiring optimization in cortical circuits. *Neuron* 34, 341–347. doi: 10.1016/S0896-6273(02)00679-7

Cohen, J. (1975). *Applied Multiple Regression/Correlation Analysis for the Behavioral Sciences/Jacob Cohen, Patricia Cohen*. Hillsdale, NJ; New York, NY: Lawrence Erlbaum Associates; distributed by Halsted Press Division of John Wiley.

Dana, H., Chen, T. W., Hu, A., Shields, B. C., Guo, C., Looger, L. L., et al. (2014). Thy1-GCaMP6 transgenic mice for neuronal population imaging *in vivo*. *PLoS ONE* 9:e108697. doi: 10.1371/journal.pone.0108697

Dempster, A. P., Laird, N. M., and Rubin, D. B. (1997). Maximum likelihood from incomplete data via the EM algorithm. *J. R. Stat. Soc. Ser. B* 39, 1–38.

Denman, D. J., and Contreras, D. (2013). The structure of pairwise correlation in mouse primary visual cortex reveals functional organization in the absence of an orientation map. *Cereb. Cortex* 24, 2707–2720. doi: 10.1093/cercor/bht128

Duda, R. O., Hart, P. E., and Stork, D. G. (2001). *Pattern Classification*. New York, NY: Wiley.

Ecker, A. S., Berens, P., Cotton, R. J., Subramaniyan, M., Denfield, G. H., Cadwell, C. R., et al. (2014). State dependence of noise correlations in macaque primary visual cortex. *Neuron* 82, 235–248. doi: 10.1016/j.neuron.2014.02.006

Ecker, A. S., Berens, P., Keliris, G. A., Bethge, M., Logothetis, N. K., and Tolias, A. S. (2010). Decorrelated neuronal firing in cortical microcircuits. *Science* 327, 584–587. doi: 10.1126/science.1179867

Golshani, P., Goncalves, J. T., Khoshkhoo, S., Mostany, R., Smirnakis, S., and Portera-Cailliau, C. (2009). Internally mediated developmental desynchronization of neocortical network activity. *J. Neurosci.* 29, 10890–10899. doi: 10.1523/JNEUROSCI.2012-09.2009

Goltstein, P. M., Montijn, J. S., and Pennartz, C. M. (2015). Effects of isoflurane anesthesia on ensemble patterns of Ca2+ activity in mouse v1: reduced direction selectivity independent of increased correlations in cellular activity. *PLoS ONE* 10:e0118277. doi: 10.1371/journal.pone.0118277

Greenberg, D. S., Houweling, A. R., and Kerr, J. N. (2008). Population imaging of ongoing neuronal activity in the visual cortex of awake rats. *Nat. Neurosci.* 11, 749–751. doi: 10.1038/nn.2140

Grippo, L., and Sciandrone, M. (2000). On the convergence of the block nonlinear Gauss-Seidel method under convex constraints. *Oper. Res. Lett.* 26, 127–136. doi: 10.1016/S0167-6377(99)00074-7

Guizar-Sicairos, M., Thurman, S. T., and Fienup, J. R. (2008). Efficient subpixel image registration algorithms. *Opt. Lett.* 33, 156–158. doi: 10.1364/OL.33.000156

Haider, B., Hausser, M., and Carandini, M. (2013). Inhibition dominates sensory responses in the awake cortex. *Nature* 493, 97–100. doi: 10.1038/nature11665

Kerlin, A. M., Andermann, M. L., Berezovskii, V. K., and Reid, R. C. (2010). Broadly tuned response properties of diverse inhibitory neuron subtypes in mouse visual cortex. *Neuron* 67, 858–871. doi: 10.1016/j.neuron.2010.08.002

Kerr, J. N., De Kock, C. P., Greenberg, D. S., Bruno, R. M., Sakmann, B., and Helmchen, F. (2007). Spatial organization of neuronal population responses in layer 2/3 of rat barrel cortex. *J. Neurosci.* 27, 13316–13328. doi: 10.1523/JNEUROSCI.2210-07.2007

Kerr, J. N., Greenberg, D., and Helmchen, F. (2005). Imaging input and output of neocortical networks *in vivo*. *Proc. Natl. Acad. Sci. U.S.A.* 102, 14063–14068. doi: 10.1073/pnas.0506029102

Kim, H., and Park, H. (2007). Sparse non-negative matrix factorizations via alternating non-negativity-constrained least squares for microarray data analysis. *Bioinformatics* 23, 1495–1502. doi: 10.1093/bioinformatics/btm134

Kim, S.-J., Koh, K., Lustig, M., Boyd, S., and Gorinevsky, D. (2007). An interior-point method for large-scale l1-regularized least squares. *IEEE J. Sel. Top. Signal Process.* 1, 606–617. doi: 10.1109/JSTSP.2007.910971

Margrie, T. W., Meyer, A. H., Caputi, A., Monyer, H., Hasan, M. T., Schaefer, A. T., et al. (2003). Targeted whole-cell recordings in the mammalian brain *in vivo*. *Neuron* 39, 911–918. doi: 10.1016/j.neuron.2003.08.012

Michelson, A. (1927). *Studies in Optics*. Chicago: University of Chicago Press.

Niell, C. M., and Stryker, M. P. (2010). Modulation of visual responses by behavioral state in mouse visual cortex. *Neuron* 65, 472–479. doi: 10.1016/j.neuron.2010.01.033

Nimmerjahn, A., Kirchhoff, F., Kerr, J. N., and Helmchen, F. (2004). Sulforhodamine 101 as a specific marker of astroglia in the neocortex *in vivo*. *Nat. Methods* 1, 31–37. doi: 10.1038/nmeth706

Ohki, K., Chung, S., Ch'ng, Y. H., Kara, P., and Reid, R. C. (2005). Functional imaging with cellular resolution reveals precise micro-architecture in visual cortex. *Nature* 433, 597–603. doi: 10.1038/nature03274

Okun, M., Steinmetz, N. A., Cossell, L., Iacaruso, M. F., Ko, H., Bartho, P., et al. (2015). Diverse coupling of neurons to populations in sensory cortex. *Nature* 521, 511–515. doi: 10.1038/nature14273

Polack, P. O., Friedman, J., and Golshani, P. (2013). Cellular mechanisms of brain state-dependent gain modulation in visual cortex. *Nat. Neurosci.* 16, 1331–1339. doi: 10.1038/nn.3464

Priebe, N. J., and Ferster, D. (2008). Inhibition, spike threshold, and stimulus selectivity in primary visual cortex. *Neuron* 57, 482–497. doi: 10.1016/j.neuron.2008.02.005

Ray, S., and Maunsell, J. H. (2010). Differences in gamma frequencies across visual cortex restrict their possible use in computation. *Neuron* 67, 885–896. doi: 10.1016/j.neuron.2010.08.004

Ringach, D. L., Mineault, P. J., Tring, E., Olivas, N. D., Garcia-Junco-Clemente, P., and Trachtenberg, J. T. (2016). Spatial clustering of tuning in mouse primary visual cortex. *Nat. Commun.* 7:12270. doi: 10.1038/ncomms12270

Rothschild, G., Nelken, I., and Mizrahi, A. (2010). Functional organization and population dynamics in the mouse primary auditory cortex. *Nat. Neurosci.* 13, 353–360. doi: 10.1038/nn.2484

Sawinski, J., Wallace, D. J., Greenberg, D. S., Grossmann, S., Denk, W., and Kerr, J. N. (2009). Visually evoked activity in cortical cells imaged in freely moving animals. *Proc. Natl. Acad. Sci. U.S.A.* 106, 19557–19562. doi: 10.1073/pnas.0903680106

Shadlen, M. N., and Newsome, W. T. (1998). The variable discharge of cortical neurons: implications for connectivity, computation, and information coding. *J. Neurosci.* 18, 3870–3896.

Smith, M. A., and Kohn, A. (2008). Spatial and temporal scales of neuronal correlation in primary visual cortex. *J. Neurosci.* 28, 12591–12603. doi: 10.1523/JNEUROSCI.2929-08.2008

Vogelstein, J. T., Packer, A. M., Machado, T. A., Sippy, T., Babadi, B., Yuste, R., et al. (2010). Fast nonnegative deconvolution for spike train inference from population calcium imaging. *J. Neurophysiol.* 104, 3691–3704. doi: 10.1152/jn.01073.2009

Waters, J., Larkum, M., Sakmann, B., and Helmchen, F. (2003). Supralinear Ca2+ influx into dendritic tufts of layer 2/3 neocortical pyramidal neurons *in vitro* and *in vivo*. *J. Neurosci.* 23, 8558–8567.

Conflict of Interest Statement: The authors declare that the research was conducted in the absence of any commercial or financial relationships that could be construed as a potential conflict of interest.